Laser and Particle Beams (2009), *27*, 19–26. Printed in the USA.

doi:10.1017/S0263034609000032

Spatial and temporal characteristics of X-ray emission from hot plasma driven by a relativistic femtosecond laser pulse

W. HONG,[1] Y. HE,[1] T. WEN,[1] H. DU,[1] J. TENG,[1] X. QING,[1,3] Z. HUANG,[2] W. HUANG,[1] H. LIU,[1] X. WANG,[1] X. HUANG,[1] Q. ZHU,[1] Y. DING,[1] AND H. PENG[1]

[1]National Key Laboratory of Laser Fusion, Research Center of Laser Fusion, China Academy of Engineering Physics, Mianyang, Sichuan Province, China
[2]Department of Engineering Physics, Tsinghua University, Haidian District, Beijing, China
[3]Physics Department, National University of Defense Technology, Changsha, China

(RECEIVED 20 June 2008; ACCEPTED 9 November 2008)

Abstract

We present the temporal and spatial characterization of X-ray sources (at ~1 keV) driven by a 200 TW, 30 fs, 800 nm laser pulse on SILEX-I laser facility at Research Center of Laser Fusion. For laser copper foil interaction with laser intensity between 6×10^{18} W/cm^2 and 3×10^{19} W/cm^2, the X-ray images show cone-like jet structures. While the yield of X-rays is strongly dependent on the laser intensity, the plasma expansion length is weakly dependent on the laser intensity, and the open angle of the cone-like jet is not correlated to the laser intensity. The formation of the jet structure is attributed to the plasma transverse confine by the self-induced quasi-static magnetic field. An X-ray pedestal 4 ns preceding the main pulse was observed. The correlation between X-ray pedestal and collimated proton beam generation was found.

Keywords: Femtosecond pulse; Plasma jet; Relativistic plasmas; Time-space-resolved; X-ray emission

INTRODUCTION

Diagnosis of X-rays has been one of the most important diagnostic methods for laser plasma study since the late 1960s, when nanosecond glass lasers grew more powerful and the inertial confined fusion (ICF) program became more active (Hora, 2007; Schwarz & Hora, 1969). Temporal, spatial, and spectroscopic characterization of X-ray emission were widely performed for the transit, high temperature, and high density laser plasma (Basov *et al.*, 1989; Faenov & Pikuz, 2003; Faenov *et al.*, 2007; Cao *et al.*, 2007), which has resulted in copious knowledge about the laser plasmas. The advent of the compact femtosecond laser in the early 1990s made it possible to study the new laser plasma interaction phenomena at very high plasma density (about solid plasma density of 10^{24}/cm^3). Extremely short pulse duration makes the expansion of the plasma negligible during interaction (Gibbon, 2005*b*). Collimated hot electron beams and ion beams were excited *via* different collisionless mechanisms under extremely high laser intensity (Kulagin *et al.*, 2008; Niu *et al.*, 2008; Flippo *et al.*, 2007; Zhou *et al.*, 2007). Strong magnetic fields play important roles in the behavior of this kind of plasmas (Wilks *et al.*, 1992; Singh & Malik, 2008; Malik *et al.*, 2008; Torrisi *et al.*, 2007). Using the X-ray spectroscopic technique, high density and high temperature characteristics of the femtosecond laser driven plasma were confirmed (Teubner *et al.*, 1996; Zhong *et al.*, 1999).

Because a focused laser beam could easily produce a very bright and short X-ray pulse, a variety of applications of ultrashort X-ray pulse is under intensive investigation (Gibbon, 2005*a*; Turcu & Dance, 1998). The applications of short pulse X-rays in microscopy (Hertz *et al.*, 2003; Rymell *et al.*, 1995), lithograph (Dusterer *et al.*, 2001), biomedical imaging (Svanberg, 2001; Kieffer *et al.*, 2002), and ultrafast probing of atomic structure (Rousse *et al.*, 2001*a*, 2001*b*), are currently studied. The characterization of the X-ray emission is the foundation for all these applications.

In this paper, the temporal and spatial characterization of the plasma X-ray source driven by the SILEX-I laser facility at CAEP (a 200 TW, 30 fs Ti:sapphire laser facility) is presented for a laser intensity between 6×10^{18} W/cm^2 and 3×10^{19} W/cm^2. For this large scale femtosecond laser facility, it is important to perform a basic characterization

Address correspondence and reprint requests to: Wei Hong, National Key Laboratory of Laser Fusion, Research Center of Laser Fusion, China Academy of Engineering Physics, P.O. Box, 919-986, Mianyang, Sichuan Province, China, 621900. E-mail: jminhong@126.com

of its X-ray emission both spatially and temporally for a laser foil target interaction before more complex experiments. The time-resolved measurement of X-ray emission by a fast X-ray diode (XRD) clearly shows a 4 ns X-ray pedestal preceding the main X-ray pulse, with varied intensities. This is due to the unstable laser prepulse and proved to have substantial impact on laser plasma applications, such as X-ray yield and proton acceleration. An X-ray pinhole CCD camera provided space-resolved information about the X-ray emission at ~keV range. The cone-like jet structure was constantly observed, similar to observations in other experiments (Schaumann *et al.*, 2005; Kasperczuk *et al.*, 2008; Sizyuk *et al.*, 2007). An interesting observation is the independence of the cone angle of the X-ray image of the laser intensity for the experimental parameter range. The quasi-static magnetic field was inferred from this observation. The quantitative correlations between laser intensity and X-ray yield and shape factors (expansion length, cone angle) are presented and interpreted. The drift of the X-ray location was measured to be within ~100 μm. The data are very useful for experiments where high alignment is required, such as the Wakefield electron acceleration using a capillary plasma channel.

EXPERIMENTAL DETAILS

The experiment was carried out on the SILEX-I laser facility (Peng, 2006) in the Laser Fusion Research Center, China Academy of Engineering Physics (CAEP). SILEX-I is a Ti:sapphire laser facility employing chirped-pulse-amplification (CPA) technique. The maximum output is 286 TW for 30 fs pulse duration at the wavelength of 800 nm. An $F/2.625$ off axis parabolic mirror (OAP, focal length = 420 mm) was used to focus the laser beam (160 mm in diameter) into a bright circular spot. The full width at half maximum (FWHM) of the focus spot is about 8 μm in which about 12% of the laser energy was contained. The maximum laser intensity reached 6.8×10^{19} W/cm^2 (1 J laser energy corresponds to a laser intensity of 1.04×10^{19} W/cm^2), which is beyond the relativistic intensity of 1.37×10^{18} μm^2 W/cm^2. The relatively low energy concentration could be improved by installing a deformable mirror. This facility routinely delivered a laser pulse with energy of more than 1 J every 25 min, while it also operates at 10 Hz at 3 TW level for the low power experiments. For normal operation, the contrast ratio is 3×10^5 for the prepulse leaking from regen-amplifier at 8.4 ns before the main pulse, and it is better than 10^6 for the amplified spontaneous emission (ASE). However, due to the instability of the pockets cell for this round of experimental campaign, a prepulse larger than usual was observed 4 ns preceding the main femtosecond pulse with varied intensities.

8-μm-thick copper foil targets were used in the experiment. Each laser pulse shot on a new piece of foil by moving a computer-controlled translation stage inside the vacuum chamber. An alignment laser telescope system was used to align the OAP and the targets.

The image of the keV X-ray emission from the laser-produced plasma was measured by an X-ray pinhole CCD camera with a 4×4 pinhole array. The array was prepared by a YAG laser on a piece of 25-μm-thick titanium foil. As the imaging element, the array of pinholes has larger view-field than a single pinhole. Each aperture is 10 μm in diameter. The apertures are covered by a 25 μm beryllium foil which blocked the scattering laser light and X-ray photons with energy less than ~1 keV. A water-cooled 512×512, 16 bit back-illuminated X-ray CCD camera (PI, SE-TE/CCD-512-TKB) recorded the X-ray image online. The quantum efficiency (QE) of the CCD chip is less than 10% for the photons with energy larger than 9 keV. Combining the QE of CCD chip and the transmission of beryllium foil, the imaging system is sensitive for 1 keV to 9 keV X-ray photons, and has highest sensitivity near 2.5 keV. The magnification factor of this imaging system was set to 8.6 and spatial resolution was 10.4 μm.

A calibrated XRD was used in the experiment to measure the time-resolved X-ray signal from the laser heated plasma. This XRD has a resolution time of ~250 ps and measures a few nanosecond time ranges. A 1.3 μm carbon filter was used for the XRD. Besides the XRD detector, an X-ray streak camera with 2 μm carbon filter was used to measure the main X-ray pulse duration. The time resolution is ~3 ps for this streak camera.

The emission of proton beams in the back of the target was measured by a piece of CR39 detector, which was parallel to the target plane. The CR39 was situated 5 cm from the target.

Figure 1 shows the schematics of the experimental setup. The *Z*-axis is the normal of the foil target. The *p*-polarized laser focused on the foil with the incident angle of 23° in the *X-Z* plane. The axis of the X-ray pinhole camera has a polar angle (θ) of 64° and an azimuth angle (φ) of 27°. The better orientation ($\theta = 90°$, $\varphi = 90°$) of the X-ray CCD camera would give more straightforward data to explain the characteristics of X-ray images, but it is not possible in our experiment due to the limits of the chamber configuration. The pictures taken by the X-ray pinhole CCD camera are consequently a projection of the three-dimensional (3D) plasma X-ray source for this particular orientation. The XRD detector was situated 50 cm from the target in the front side of the target (the side which the laser impinged on).

RESULTS AND DISCUSSION

Spatial Characteristics

The X-ray pinhole CCD camera is easy to align and very stable in the collection of experimental data. Data for more than 50 shots in a two-week experimental campaign have been obtained for copper foils. Only 5% of the data

https://doi.org/10.1017/S0263034609000032 Published online by Cambridge University Press

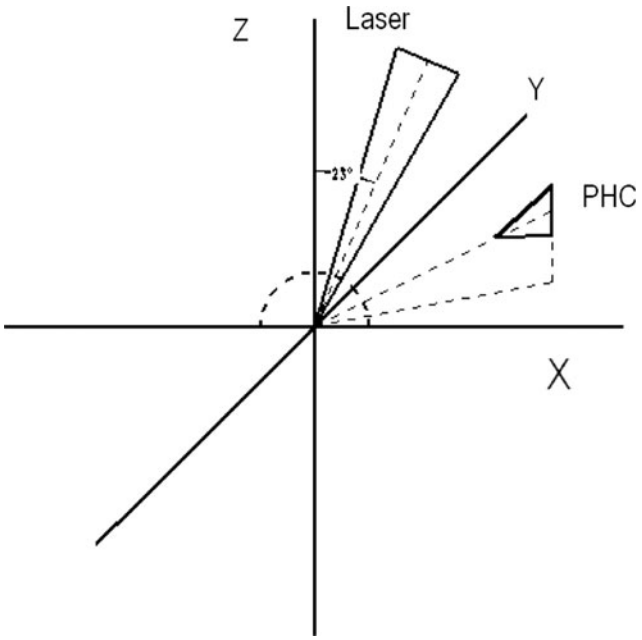

Fig. 1. The schematics of the experimental setup. PHC stands for the pinhole camera. The *Z*-axis is the normal of the foil target. The *X*-*Z* plane is the laser incident plane. The laser incident angle is 23°. The axis of pinhole camera has an angle of 64° to the *Z*-axis and an azimuth angle of 27°.

showed no X-ray image, which was due to the failure of the laser facility.

A typical keV X-ray image from the X-ray CCD camera is shown in Figure 2a. The laser energy was 2.27 J (1.51×10^{19} μm^2 W/cm^2). This image is easy to understand if we assume that the X-ray source has a cone-like jet structure. This assumption is supported by the following analysis. Although the surface of the target foil is not visible in Figure 2a, the direction of the target normal could be determined from the intensity distribution of the X-ray image. The intensity profile was obtained for the directions *P* and *N* for the X-ray image in Figure 2a using Winview 3.1 software and shown in Figures 2b and 2c. The correction for the view angle of the pinhole camera was already considered. The origin in Figures 2b and 2c is the location of the brightest spot of the X-ray image. In Figure 2b, the curve shows good symmetry about the curve peak, while the curve in Figure 2c clearly shows asymmetry about the curve peak. The FWHM for curves in Figures 2b and 2c are 35 μm and 33 μm, respectively.

For the intense femtosecond laser impinging on the solid target surface, the absorption of laser occurred mostly at the steepened critical surface of plasma *via* different collisionless absorption processes. The brightest spot in the X-ray image corresponds to the high temperature and high density region near the critical surface. When the heated plasma expands into the vacuum, the target normal direction will be one rotational symmetric axis for the expanded plasma. This symmetric character leads to the conclusion that the *P* direction is parallel to the target surface according

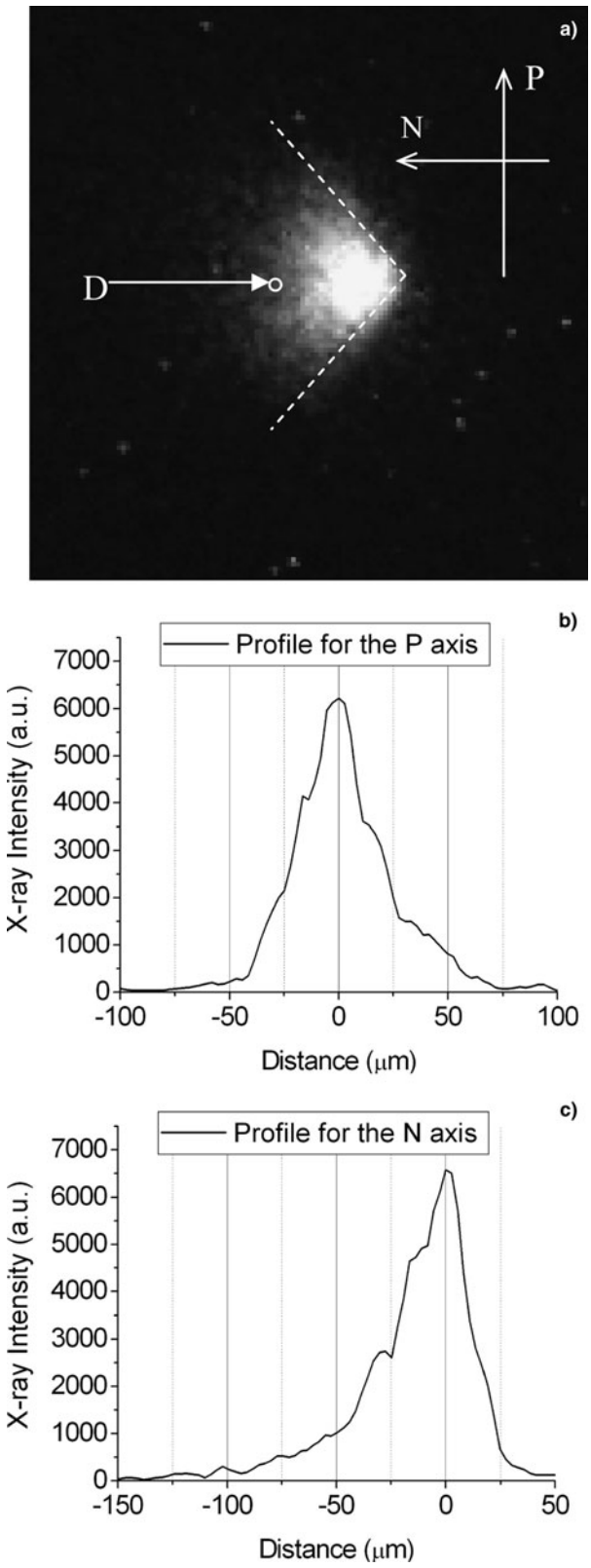

Fig. 2. The keV X-ray emission image taken with an X-ray pinhole camera for a focused femtosecond laser and foil interaction (**a**). The *P* axis is parallel to the foil surface and the *N* axis is perpendicular to foil surface. The white circle indicates the position of characteristic pixel D, which has counts of ~500. The profiles for *P* and *N* directions are shown in (**b**) and (**c**). The FWHM for curves in (b) and (c) are 35 μm and 33 μm, respectively.

https://doi.org/10.1017/S0263034609000032 Published online by Cambridge University Press

to the symmetric curve in Figure 2b, and the *N* direction is the project of the target normal on the CCD chip plane. Considering well-known temperature and density distributions for the expanded laser plasma (Kruer, 2003; Wilks *et al.*, 1992), it is readily understood that the left long tail in the Figure 2c represents the vacuum side that the plasma expands into.

To further understand the characteristics of the X-ray image in Figure 2a, we hereby define two quantities. The first one is the cone angle Θ as indicated by the two dashed lines in Figure 2a, the counts recorder by the pixels on the dashed line is ∼10% of the counts of the brightest pixel on whole image. This cone angle is an indicator of the expansion of the plasma in the transverse direction. The second quantity is the expansion length *L*, which is defined as the distance from the brightest pixel (labeled as pixel B) to a characteristic pixel (labeled as pixel D) along the *N* direction. The count recorded by pixel D has a constant number of ∼500. For the image in Figure 2a, Θ and *L* are 86° and 86 μm, respectively.

Expansion Lengths

With fixed laser pulse duration and focus condition, we have studied the Θ and *L* dependence on the laser energy. Figures 3 and 4 shows the expansion length and cone angle data for a total of 17 shots. In Figure 3, when the laser energy increases from 0.8 J to 2.6 J, the expansion length shows a positive correlation to the laser energy. The maximum length reached is 102 μm. To quantitatively describe the function

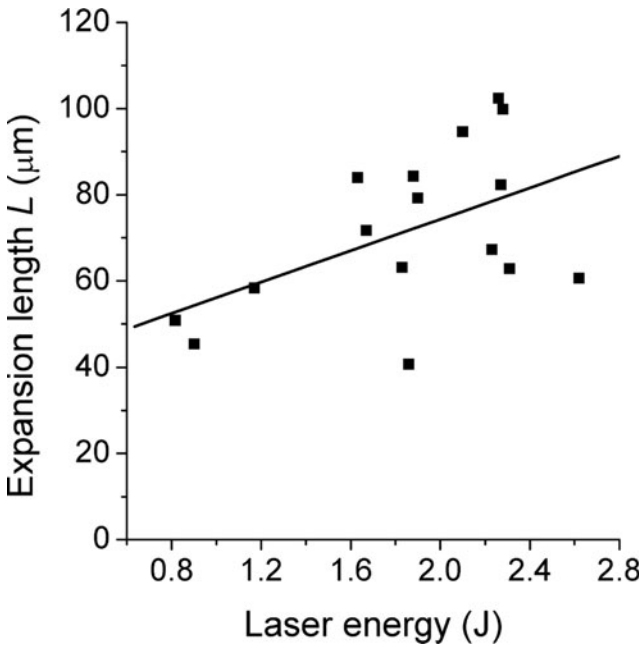

Fig. 3. Dependence of expansion length *L* on laser energy. The square dots are experimental data. The solid line is the indication of the trend for the eyes. The laser pulse is a 30 FS one.

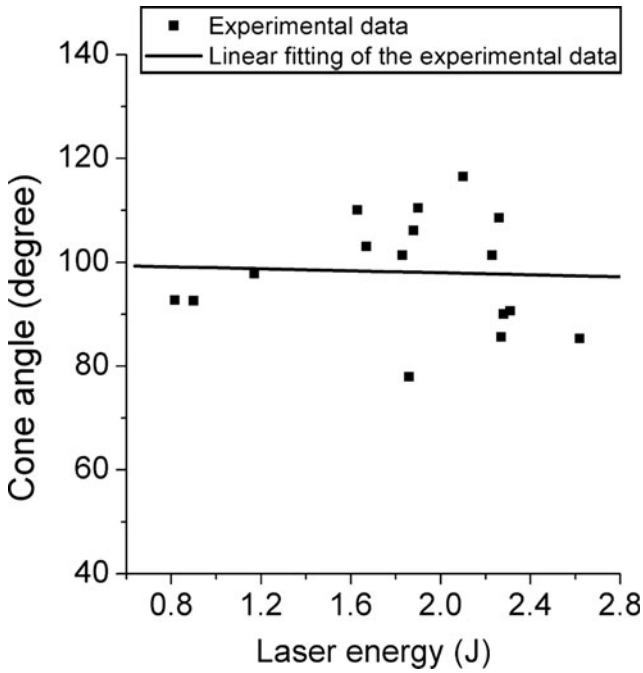

Fig. 4. The dependence of cone angle Θ on laser energy. The solid line describes the linear fitting of experimental data. The laser pulse is a 30 FS one.

of the expansion length on the laser intensity requires the description of many physical processes, such as the laser absorption, expansion hydrodynamics, X-ray emission, and absorption. Here, we just use a straight line to indicate the positive correlation of expansion length to laser energy in Figure 3; however, we have to notice that the correlation between expansion and laser energy is relatively weak, 300% increase of laser energy leads to only 60% increase of expansion length. We suggest that one factor contributing to this observation is the high plasma density for short pulse laser interactions. The high density plasma has high collision and recombination rates, and therefore also short plasma decay time and expansion length. On the other hand, from Figure 3, it is clear that the data of expansion length are rather scattering for similar laser energy. For example, the expansion lengths varied from 61 μm to 102 μm at laser energy around 2.3 J for five different shots. This scattering of data suggests that other factors also contribute to the expansion length. Both uncertainty of laser intensity and prepulse can cause the variation of expansion length. According to the experimental data, the standard error of the laser intensity for our laser system is ±15% due to the variation of laser focus size and concentration for fixed laser energy and fixed pulse duration. The prepulse also strongly influences the laser absorption and X-ray emission (Cobble *et al.*, 1991; Zhidkov *et al.*, 2000; Laska *et al.*, 2007). The prepulse has direct control over the scale length of the preformed plasma and may greatly enhance the laser absorption, and therefore the production of the X-ray. The duration of the X-ray pulse is always longer when the prepulse is present (Murnane

https://doi.org/10.1017/S0263034609000032 Published online by Cambridge University Press

et al., 1989; Kulcsár, 2000). If we use the ion acoustic velocity (c_s) to estimate the expansion length, $L = \tau \times c_s$, where τ is the X-ray pulse duration, $c_s \propto (Z \times T_e/M)^{1/2}$ is a function of plasma temperature and therefore laser intensity, the longer X-ray pulse corresponds to the longer expansion length for the same laser intensity. We found that the prepulse in the nanosecond scale has substantial variation for the SILEX-I laser system, this greatly accounts for the scattering of the expansion length.

Cone Angles

The cone angles are almost independent of the laser energy as shown in Figure 4. The solid line that linearly fits the experimental data is almost parallel to the horizontal axis. The cone angles fluctuated between 78° to 116°. The average value is ~100°. These data generally agree with the previous studies where a cone-like jet structure has been observed. The Burgess's results (Burgess *et al.*, 1985) showed that the 20 ps laser driven plasma at laser intensity of 3×10^{17} W/cm^2 exhibited a cone-like jet expansion into the vacuum. Their interference measurement with a probe laser gave the cone angle of 50° for all ions and 20° for the fast ions. Li *et al.* (2000) have also observed the plasma jet structure for the 100 fs laser solid target interaction at laser intensity of 5×10^{15} W/cm^2 with the Nomarski interference technique. The basic physical concept to explain the formation of these jets is the transit quasi-static magnetic field formed during the short pulse laser target interaction. This quasi-static magnetic field has been studied by both particle-in-cell simulation (Wilks *et al.*, 1992) and experiment (Stamper *et al.*, 1978). The specific cone angle could generally be determined by the balance between thermal pressure of plasma and magnetic pressure. This balance condition is specified by the equation $B^2 = 8\pi n_e k T_e$, where B is the magnetic field, n_e is the plasma density, and T_e is the electron temperature (in CGS units). The independence of the cone angle of the laser energy could be explained by the reasonable assumption that T_e and B simultaneous increase with the laser energy. So, the balance point of plasma thermal pressure and magnetic pressure does not vary much for our experimental laser energy range. In other words, the cone angle is almost a constant.

X-ray Yields

The yield of the X-ray emission is an important quantity for practical application. The pixel with largest counts in each X-ray image was picked-up and the average count for the 25 pixels (5 × 5) near this brightest pixel was calculated. The average count is approximated as the yield of each X-ray pulse and is shown in Figure 5 as a function of laser energy. This approximation has ignored the difference in terms of X-ray source size, distribution, and spectrum for different laser intensity. If we assume that the X-ray radiation from the femtosecond laser plasma is nearly a black body

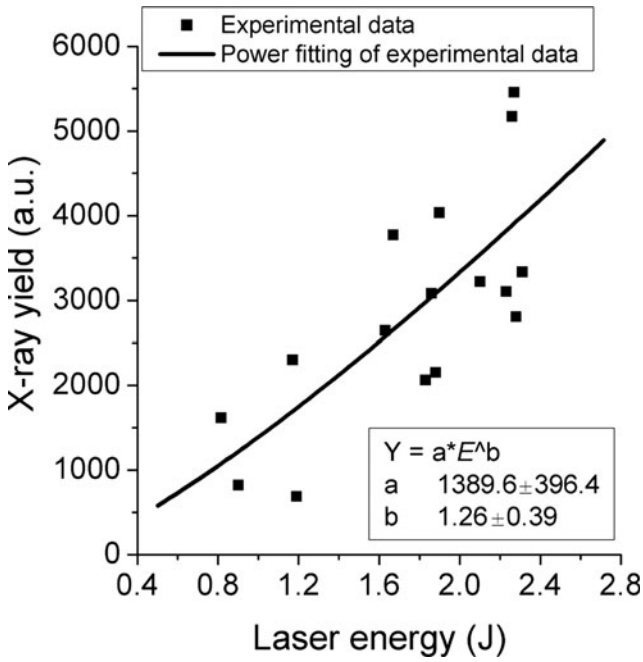

Fig. 5. Dependence of X-ray yield on laser energy. The X-ray yield is represented by the average counts of the 25 neighboring pixels with largest counts. The solid line shows the power fitting of experimental data.

radiation, according to the Stefan-Boltzmann radiation power relation $\sigma_B T_e^4$, and using the empirical approximation that the electron temperature scales roughly as $I^{1/3}$ (Jiang *et al.*, 1995), the X-ray yield is proportional to $I^{4/3}$. Our fitting of experimental data using the power function gives a relation of $Y = 1389 \times E^{1.26 \pm 0.39}$, where Y is the X-ray yield and E is the laser energy. This good agreement suggests that the thermal equilibrium has almost reached in the case of the high density plasma during very short X-ray emission time. Comparing Figure 3 and Figure 5, we found that when the laser energy increased by a factor of about 3, the expansion length only increased by a factor of 1.6, however, the counts of brightest X-ray spot increased by a factor of ~4. Obviously, the X-ray yield depends stronger on the laser energy. By increasing the laser energy, it is possible to increase the brightness of the X-ray source while keeping its relative small size. This shows the advantage of femtosecond laser plasma as small size, high brightness X-ray sources.

Drift of X-ray Source Positions

The stability of X-ray image positions is another aspect that we have studied. The coordinates of the brightest X-ray spots for 17 shots were summarized in Figure 6. The N and P directions are defined as in Figure 2. For the P direction, the X-ray position varied between ±60 μm, which corresponds to the direction drift of ±143 μrad for the OAP with focus length of 420 mm. The point instability of the laser beam is only ±20 μrad according to the other independent experimental

https://doi.org/10.1017/S0263034609000032 Published online by Cambridge University Press

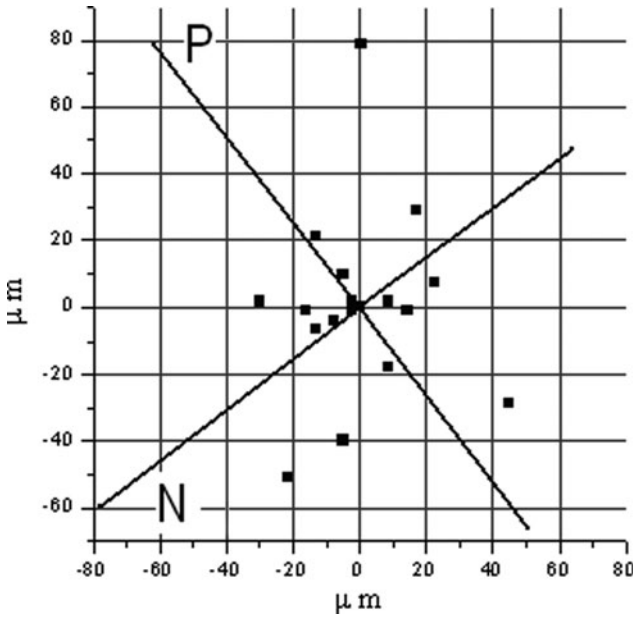

Fig. 6. The positions of the brightest X-ray spots for a series of laser shots. The position uncertainties for the *N* direction and the *P* direction are ± 40 μm and ± 60 μm, respectively.

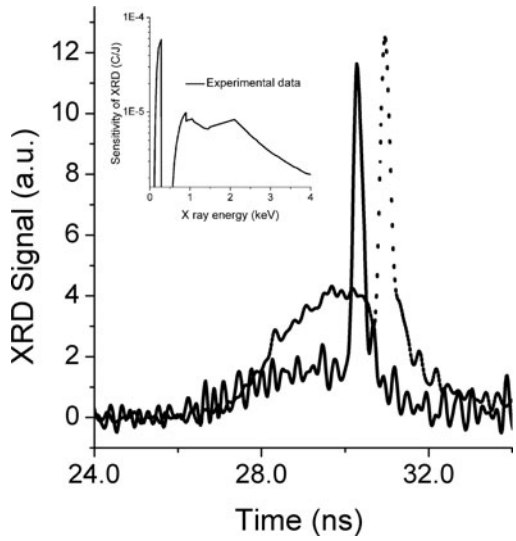

Fig. 7. The time-resolved XRD signals for two separate shots (solid and dashed line) that show varied X-ray pedestals. The laser energy is 3.15 J for solid line and 3.34 J for dashed line. The inset shows the calibrated sensitivity curve for the XRD with 1.3 μm carbon filter.

measurement. We suggest that the uncertainty during the alignment of OAP may contribute to the big variation of X-ray spots in the *P* direction. For the *N* direction, the X-ray position varied between ± 40 μm. Several factors will cause this uncertainty. First, when the targets were aligned with alignment laser, the alignment accuracy was 30 μm. Second, due to a different prepulse for each shot, the position of the critical density surface, to which the brightest X-ray spots are closely located, was different when the femtosecond laser pulse arrived. Finally, the instability of the laser self-focusing near the focus position may also have some connection to the uncertainty for the *N* direction.

Temporal Characteristics

The temporal behavior of the X-ray emission from the laser heated plasma for the nanosecond time scale was measured with a calibrated XRD. The high voltage applied to the XRD detector equaled 1 kV, and a Tektronix TDS694C oscilloscope was used to record the data. The inset in Figure 7 shows the sensitivity of the XRD for the photon energy up to 4 keV with a 1.3 μm carbon filter. The calibration was carried out on the Beijing Synchrotron Radiation Facility. The XRD has a sensitive band near carbon K-edge at ∼280 eV, and is almost constant for 1–2 keV. As demonstrated by two typical XRD signal curves in Figure 7, besides the main X-ray peak with FWHM of 270 ps, a strong pedestal started about 4 ns preceding the main pulse. The duration of the main peak is ∼40 ps according to the X-ray streak camera data (will be published elsewhere). The measured 270 ps FWHM are mostly determined by the time resolution of the XRD detector system. Due to different laser intensity for the main pulse and the laser prepulse ($\sim 10^{18}$ W/cm^2 *vs.* $\sim 10^{13}$ W/cm^2), the X-rays in the main pulse part are harder (higher energy) than in the pedestal part. We suggest that the X-ray pedestal is mainly caused by the X-ray photons within the 280 eV sensitive band of XRD. Because the pedestal lasts more than 4 ns, the duration of laser prepulse lasted probably also several nanoseconds. The intensity of pedestal varied from shot to shot. In Figure 7, for the similar laser energy (therefore similar main X-ray pulse), the pedestal of the dashed line is much stronger than that of the solid line. This fluctuation is found due to the unusual jitter of the pockets cell.

The difference of the prepulse has critical effects on some physical results. For example, a collimated proton beam was observed for the shot that gave the solid curve in Figure 7, but no proton beam was observed for the shot that gave the dashed curve in Figure 7. Kaluza *et al.* (2004) have systematically studied the influence of the prepulse on the proton acceleration. Our results provided additional evidence supporting their results and showed that a very strong prepulse completely destroys the acceleration electrical field for the Target Normal Sheath Acceleration laser proton acceleration scheme (Snavely *et al.*, 2000). Control over the prepulse is essential to obtain the high energy laser proton beams in the future.

CONCLUSIONS

The X-ray emission of relativistic plasma has been characterized spatially and temporally. The cone-like jet structure is the basic characteristic of the expansion of the plasma in

https://doi.org/10.1017/S0263034609000032 Published online by Cambridge University Press

the femtosecond laser foil interaction. The laser intensity and the prepulse both play important roles in the X-ray generation and plasma expansion. The quasi-static magnetic field has pinched the expanded plasma in the transverse direction. The balance between the thermal pressure of the plasma and the magnetic pressure leads to the independence of the cone angle of the laser intensity. The XRD signal has revealed the fluctuation of the nanosecond prepulse of the laser system. Our work shows the basic characters of the SILEX-I facility. It provides the bases to improve the prepulse and stability of the facility. The data is also very important for the X-ray radiography where size and intensity of the X-ray source are crucial for high spatial resolution radiography.

ACKNOWLEDGEMENT

This work was supported at Research Center of Laser Fusion, CAEP, by the National Science Foundation Committee (Grant No. 10775121, 10774133), the National Key Laboratory of Laser Fusion (Grant No. 9140C6802030603), and the LFRC Innovation Foundation (Grant No. 200407)

REFERENCES

Basov, N.G., Zakharenkov, Y.A., Rupasov, A.A., Sklizkov, G.V. & Shikanov, A.S. (1989). *Dense Plasma Diagnostics*. Moscow: Nauka.

Burgess, M.D.J., Luther-Davis, B. & Nugent, K.A. (1985). An experimental study of magnetic fields in plasmas created by high intensity one micro laser radiation. *Phys. Fluids*. **28**, 2286–2297.

Cao, L.F., Uschmann, I., Zamponi, F., Kampfer, T., Fuhrmann, A., Forster, E., Holl, A., Redmer, R., Toleikis, S., Tschentscher, T. & Glenzer, S.H. (2007). Space-time characterization of laser plasma interactions in the warm dense matter regime. *Laser Part. Beams* **25**, 239–244.

Cobble, J.A., Schappert, G.T., Jones, L.A., Taylor, A.J., Kyrala, G.A. & Fulton, R.D. (1991). The interaction of a high irradiance, subpicosecond laser pulse with aluminum: The effects of the prepulse on X-ray production. *J. Appl. Phys*. **69**, 3369–3371.

Dusterer, S., Schwoerer, H., Ziegler, W., Ziener, C. & Sauerbrey, R. (2001). Optimization of EUV radiation yield from laser-produced plasma. *Appl. Phys. B* **73**, 693–698.

Faenov, A.Y. & Pikuz, T.A. (2003). *Atoms and Plasmas in Super-Intense Laser Fields*. Sicily: Erice.

Faenov, A.Y., Magunov, A.I., Pikuz, T.A., Skobelev, I.Y., Gasilov, S.V., Stagira, S., Calegari, F., Nisoli, M., De Silvestri, S., Poletto, L., Villoresi, P. & Andreev, A.A. (2007). X-ray spectroscopy observation of fast ions generation in plasma produced by short low-contrast laser pulse irradiation of solid targets. *Laser Part. Beams* **25**, 267–275.

Flippo, K., Hegelich, B.M., Albright, B.J., Yin, L., Gautier, D.C., Letzring, S., Schollmeier, M., Schreiber, J., Schulze, R. & Fernandez, J.C. (2007). Laser-driven ion accelerators: Spectral control, monoenergetic ions and new acceleration mechanisms. *Laser Part. Beams* **25**, 3–8.

Gibbon, P. (2005*a*). *Short Pulse Laser Interactions with Matter: An Introduction*. London: Imperial College Press.

Gibbon, P. (2005*b*). *Short Pulse Laser Interactions with Matter: An Introduction*. London: Imperial College Press.

Hertz, H.M., Johansson, G.A., Stollberg, H., De Groot, J., Hemberg, O., Holmberg, A., Rehbein, S., Jansson, P., Eriksson, F. & Birch, J. (2003). Table-top X-ray microscopy: Sources, optics and applications. *J. Phys. IV* **104**, 115–119.

Hora, H. (2007). New aspects for fusion energy using inertial confinement. *Laser Part. Beams* **25**, 37–45.

Jiang, Z., Kieffer, J.C., Matte, J.P., Chaker, M., Peyrusse, O., Giiles, D., Korn, G., Maksimchuk, A., Coe, S. & Mourou, G. (1995). X-ray spectroscopy of hot solid density plasmas produced by subpicosecond high contrast laser pulses at 10^{18}–10^{19} W/cm^2. *Phys. Plasmas* **2**, 1702–1711.

Kaluza, M., Schreiber, J., Santala, M.I., Tsakiris, G.D., Eidmann, K., Meyer-Ter-Vehn, J. & Witte, K.J. (2004). Influence of the laser prepulse on proton acceleration in thin-foil experiments. *Phys. Rev. Lett*. **93**, 045003.

Kasperczuk, A., Pisarczyk, T., Kalal, M., Martinkova, M., Ullschmied, J., Krousky, E., Masek, K., Pfeifer, M., Rohlena, K., Skala, J. & Pisarczyk, P. (2008). PALS laser energy transfer into solid targets and its dependence on the lens focal point position with respect to the target surface. *Laser Part. Beams* **26**, 189–196.

Kieffer, J.C., Krol, A., Jiang, Z., Chamberlain, C.C., Scalzetti, E. & Ichalalene, Z. (2002). Future of laser-based X-ray sources for medical imaging. *Appl. Phys. B*. **74**, S75–S81.

Kruer, W.L. (2003). *The Physics of Laser Plasma Interactions*. Boulder, Co: Westview Press.

Kulagin, V.V., Cherepenin, V.A., Hur, M.S., Lee, J. & Suk, H. (2008). Evolution of a high-density electron beam in the field of a super-intense laser pulse. *Laser Part. Beams* **26**, 397–409.

Kulcsár, G., Budnik, F.W., Herman, P.R., Moskovits, M., Zhao, L. & Marjoribanks, R.S. (2000). Intense picosecond X-ray pulses from laser plasmas by use of nanostructured "velvet" targets. *Phys. Rev. Lett*. **84**, 5149.

Laska, L., Badziak, J., Gammino, S., Jungwirth, K., Kasperczuk, A., Krasa, J., Krousky, E., Kubes, P., Parys, P., Pfeifer, M., Pisarczyk, T., Rohlena, K., Rosinski, M., Ryc, L., Skala, J., Torrisi, L., Ullschmied, J., Velyhan, A. & Wolowsk, J. (2007). The influence of an intense laser beam interaction with preformed plasma on the characteristics of emitted ion streams. *Laser Part. Beams* **25**, 549–556.

Li, Y.T., Zhang, J.I., Chen, L.M., Xia, J.F., Teng, H., Wei, Z.Y. & Jiang, W.M. (2000). Observation of the transverse pinch of the expansion of an femtosecond laser plasma. *Acta Phys. Sini*. **49**, 1400–1403.

Malik, H.K., Kumar, S. & Singh, K.P. (2008). Electron acceleration in a rectangular waveguide filled with unmagnetized inhomogeneous cold. *Laser Part. Beams* **26**, 197–205.

Murnane, M.M., Kapteyn, H.C. & Falcone, R.W. (1989). High density plasmas produced by ultrafast laser pulses. *Phys. Rev. Lett*. **62**, 155–158.

Niu, H.Y., He, X.T., Qiao, B. & Zhou, C.T. (2008). Resonant acceleration of electrons by intense circularly polarized Gaussian laser pulses. *Laser Part. Beams* **26**, 51–59.

Peng, H.S. (2006). SILEX-I:300-TW Ti:sapphire laser. *Laser Phys*. **16**, 244–247.

Rousse, A., Rischel, C. & Gauthier, J.C. (2001*b*). Colloquium: Femtosecond X-ray crystallography. *Rev. Mod. Phys*. **73**, 17–31.

Rousse, A., Rischel, C., Fourmaux, S., Uschmann, I., Sebban, S., Grillon, G., Balcou, P., Forster, E., Geindre, J.P., Audebert, P., Gauthier, J.C. & Hulin, D. (2001*a*). Non-thermal melting in semiconductors measured at femtosecond resolution. *Nat*. **410**, 65–68.

Rymell, L., Berglund, M. & Hertz, H.M. (1995). Debris-free single-line laser plasma X-ray source for microscopy. *Appl. Phys. Lett*. **66**, 2625–2627.

Schaumann, G., Schollmeier, M.S., Rodriguez-Prieto, G., Blazevic, A., Brambrink, E., Geissel, M., Korostiy, S., Pirzadeh, P., Roth, M., Rosmej, F.B., Faenov, A.Y., Pikuz, T.A., Tsigutkin, K., Maron, Y., Tahir, N.A. & Hoffmann, D.H.H. (2005). High energy heavy ion jets emerging from laser plasma generated by long pulse laser beams from the NHELIX laser system at GSI. *Laser Part. Beams* **23**, 503–512.

Schwarz, H. & Hora, H. (1969). *Laser Interaction and Related Plasma Phenomena*, Vol. 1 (Schwarz, H. & Hora, H., eds.). New York: Plenum Press.

Singh, K.P. & Malik, H.K. (2008). Resonant enhancement of electron energy by frequency chirp during, laser acceleration in an azimuthal magnetic field in a plasma. *Laser Part. Beams* **26**, 363–369.

Sizyuk, V., Hassanein, A. & Sizyuk, T. (2007). Hollow laser self-confined plasma for extreme ultraviolet lithography and other applications. *Laser Part. Beams* **25**, 143–154.

Snavely, R.A., Key, M.H., Hatchett, S.P., Cowan, T.E., Roth, M., Phillips, T.W., Stoyer, M.A., Henry, E.A., Sangster, T.C., Singh, M.S., Wilks, S.C., Mackinnon, A., Offenberger, A., Pennington, D.M., Yasuike, K., Langdon, A.B., Lasinski, B.F., Johnson, J., Perry, M.D. & Campbell, E.M. (2000). Intense high-energy proton beams from petawatt-laser irradiation of solids. *Phys. Rev. Lett*. **85**, 2945.

Stamper, J.A., Mclean, E.A. & Ripin, B.H. (1978). Studies of spontaneous magnetic fields in laser-produced plasma by Faraday rotation. *Phys. Rev. Lett*. **40**, 1177–1181.

Svanberg, S. (2001). Some applications of ultrashort laser pulses in biology and medicine. *Meas. Sci. Tech*. **12**, 1777–1783.

Teubner, U., Missalla, T. & Uschmann, I. (1996). X-ray spectra from highly ionized dense plasma produced by ultrashort laser pulses. *Appl. Phys. B*. **62**, 213–220.

Torrisi, L., Margarone, D., Gammino, S. & Ando, L. (2007). Ion energy increase in laser-generated plasma expanding through axial magnetic field trap. *Laser Part. Beams* **25**, 453–464.

Turcu, I.C.E. & Dance, J.B. (1998). *X-rays From Laser Plasmas: Generation and Applications*. New York: John Wiley & Sons.

Wilks, S.C., Kruer, W.L., Tabak, M. & Langdon, A.B. (1992). Absorption of ultra-intense laser pulses. *Phys. Rev. Lett*. **69**, 1383–1386.

Zhidkov, A., Sasaki, A., Utsumi, T., Fukumoto, I.I., Tajima, T., Saito, F., Hironaka, Y., Nakamura, K.G., Kondo, K. & Yoshida, M. (2000). Prepulse effects on the interaction of intense femtosecond laser pulses with high-Z solids. *Phys. Rev. E* **62**, 7232–40.

Zhong, F., Deng, J., Zhang, Z., Qing, L.I. & Xu, Z. (1999). Characteristic of plasma X-ray emissions generated by femtosecond and nanosecond laser pulses. *Acta Opt. Sini*. **19**, 364–368.

Zhou, C.T., Yu, M.Y. & He, X.T. (2007). Electron acceleration by high current-density relativistic electron bunch in plasmas. *Laser Part. Beams* **25**, 313–319.